Optimized Synchronization Design for UAV Swarm Network Based on Sidelink

Hang Zhang , Hua-Min Chen * , Qi-Jun Wei , Zhu-Wei Wang , Yan-Hua Sun

Posted Date: 27 February 2026

doi: 10.20944/preprints202602.1239.v1

Keywords: UAV relaying; Synchronization; 2-step RACH; sidelink; doppler shift; A-NOMA

 doi:10.20944/preprints202602.1239.v1

Article

Optimized Synchronization Design for UAV Swarm Network Based on Sidelink

Hang Zhang [1], Hua-Min Chen [1,*], Qi-Jun Wei [2,*], Zhu-Wei Wang [1] and Yan-Hua Sun [1]

[1] School of Information Science and Technology Beijing University of Technology
[2] Hangzhou UPivot Tech. Co., Ltd.
* Correspondence: chenhuamin@bjut.edu.cn (H.-M.C.); qijun.wei@upivot.cn (Q.-J.W.)

Abstract

With the deployment and application of the fifth-generation communication technology as well as the research on the sixth-generation communication technology, the space-air-ground-sea integrated network has emerged as a key vision for future communications. Unmanned aerial vehicles (UAVs), serving as aerial nodes, can be utilized in emergency rescue and disaster relief, mapping, environmental monitoring, and enhancement of communication coverage, among other areas. In terms of enhancing communication coverage, the integrated space-ground network, with UAVs as an important component, can provide seamless communication coverage to remote areas, deserts, oceans, and other all-domain three-dimensional spaces. UAVs have become important research objects due to their low cost and high flexibility, and the enhancement of communication coverage in the form of base station-relay UAV-slave UAV based on one-hop relaying has become a significant direction. However, the high mobility and extensive coverage of UAVs also give rise to synchronization challenges. In this work, to tackle the challenges of round-trip delay (RTD) from long-distance transmission and Doppler frequency offset in uplink synchronization between ground base stations and relay UAVs, a long-range random access preamble design is proposed. An enhanced two-step detection framework is introduced, where two distinct root sequence preambles are utilized for RTD estimation and random access respectively, and Doppler frequency offset is mitigated via pre-compensation. For the uplink synchronization in the sidelink between slave UAVs and relay UAVs, to address Doppler frequency offset, improve access efficiency, reduce resource consumption, and simultaneously account for the asynchrony among different users, an asynchronous non-orthogonal multiple access (A-NOMA)-based two-step random access scheme is developed. The scheme leverages existing physical random access channel (PRACH) preamble sequences with paired indexing for Doppler frequency offset estimation; on this basis, a successive interference cancellation algorithm based on Doppler frequency offset and phase compensation is designed to demodulate user data. For downlink synchronization between slave UAVs and relay UAVs, improvements to frequency offset estimation are achieved through redesigned sidelink synchronization signal block (S-SSB) resource allocation. Alongside this, a down-sampling-based detection scheme is designed to reduce UAV power consumption given energy constraints, with a comprehensive link algorithm developed to support implementation.

Keywords: UAV relaying; Synchronization; 2-step RACH; sidelink; doppler shift; A-NOMA

1. Introduction

With the large-scale commercialization of fifth-generation wireless communication technology, high-speed, high-capacity, low-latency terrestrial networks have provided comprehensive and diversified services for production and daily life [1,2]. To meet the continuous increase in application types and the exponential growth of users and data volume, research into sixth-generation wireless communication technology has been initiated by the industry [3,4]. Sixth-generation (6G) networks are envisioned to build ubiquitous, intelligently connected, secure, and flexible integrated space-air-ground

 doi:10.20944/preprints202602.1239.v1

networks [5]. Non-terrestrial networks (NTNs), recognized by the International Telecommunication Union (ITU) as a key enhancement technology for wireless communication networks due to their significantly wider coverage capabilities surpassing terrestrial networks, are driving the core vision and momentum of 6G development [6,7]. Their integrated development with terrestrial networks aims to achieve seamless three-dimensional coverage across land, sea, and air, forming a space-air-ground integrated network (SAGIN) where terrestrial networks serve as the foundation and NTNs provide the extension [8,9].

The space-air-ground integrated network is categorized into three segments: space, air, and ground networks [10,11]. Terrestrial networks, typically composed of ground base stations and IoT devices with cells as the basic unit [12], face challenges in providing effective communication coverage to remote areas such as deserts, rainforests, and oceans due to deployment difficulties and cost constraints [13,14]. The space network is formed by multiple satellites of different types and orbits, creating a multi-layer, multi-connectivity communication system to provide high-speed, reliable, and continuous communication services for aerial and terrestrial users [15,16]. The aerial network is constituted by UAVs and high-altitude platforms (HAPs), deployed in the air to collaborate with ground stations or satellites, providing broader communication coverage and higher quality communication performance [17,18]. UAVs, in particular, are considered highly valuable for applications like emergency communications and remote sensing [19], as they can offer real-time ground coverage or act as relay nodes to enhance the coverage and performance of terrestrial networks [20]. This characteristic exactly forms a complement to the shortcomings of current fifth-generation (5G) networks; therefore, the application research of UAV communication in 5G scenarios has become an important exploration direction for the industry to break through the limitations of terrestrial networks.

5G communication technology is characterized by high transmission rates, high reliability, and low latency [21]. However, due to severe attenuation at high operating frequencies, the coverage radius of a 5G base station is typically limited to only a few hundred meters [20]. Consequently, a dense deployment of 5G base stations is required to achieve comprehensive coverage. UAVs, featuring high mobility, low cost, and great flexibility, offer a solution [22]. Their integration with terrestrial 5G communication networks can overcome the limited coverage of 5G base stations, enabling the construction of aerial base stations with 5G communication capabilities to provide high-speed, low-latency, and wide-coverage communication services [23,24].

In the future, unmanned aerial vehicle (UAV) swarm communication will become a new development trend. A UAV swarm usually consists of one relay UAV and several slave UAVs. Swarm communication refers to the communication between the relay UAV and the slave UAVs. In addition, there is also a communication link between the relay UAV and the ground station. In base station-to-relay UAV-to-slave UAV communication, uplink and downlink synchronization is recognized as the initial step for users to establish connections with the base station. The high mobility of UAVs and the requirements for long-distance communication pose significant challenges to the synchronization process [25]. Furthermore, the limited on-board energy of UAVs imposes stringent requirements on the computational complexity in the synchronization process. Regarding synchronization between the relay UAV and the slave UAV, the following contributions are made in this paper:

- In terms of uplink synchronization between the relay UAV and the slave UAV, to improve spectrum efficiency and random access efficiency, this paper proposes an asynchronous non-orthogonal multiple access (A-NOMA)-enhanced two-step random access framework tailored for UAV networks. A preamble structure based on superimposed paired index sequences is designed to realize joint estimation of carrier frequency offset and transmission delay. During the data demodulation phase, joint frequency offset estimation and compensation can be completed without relying on prior frequency offset information, and this scheme is suitable for highly dynamic UAV application scenarios. A complete scheme design process and simulation analysis results are presented in this paper.

 doi:10.20944/preprints202602.1239.v1

- In response to the downlink synchronization problem between the relay UAV and the slave UAV, this paper proposes a lightweight synchronization signal detection scheme based on down-sampling to reduce the computational complexity of synchronization detection. In addition, to enhance the universality of the synchronization signal block, the structure of the sidelink synchronization signal block (S-SSB) is redesigned to support flexible configuration, enabling it to adapt to a wider range of scenarios. Furthermore, this paper elaborates on the principle of the demodulation algorithm under the aforementioned scenario, constructs a full-link simulation verification platform, and performs corresponding simulation performance analysis.

The thesis is divided into five chapters in total. Section 2 is dedicated to reviewing the research on uplink synchronization and downlink synchronization carried out by various scholars in recent years. The system model and design details are introduced in Section 3. In Section 4, the design described in Section 3 is subjected to simulation evaluation. Finally, the conclusions are summarized in Section 5.

2. Related Work

Current wireless communication networks primarily serve user equipment through terrestrial infrastructure but face limitations in remote areas such as oceans, deserts, and rainforests. Non-terrestrial networks (NTNs) composed of satellites and UAVs are recognized as an effective solution [26]. However, NTN communications introduce new challenges: long transmission distances and high relative velocities between aerial platforms and ground devices severely impact preamble detection and timing during random access, while massive device connectivity escalates collision probability and latency.

Preamble structure redesign is regarded as a promising approach to overcome frequency offsets and achieve precise timing. A novel random access preamble design for high Doppler shifts in non-terrestrial networks was proposed by [27]. Signals were generated by superimposing LFM waveforms with distinct phase offsets in the frequency domain, enabling preamble detection and timing estimation to be achieved under severe Doppler conditions. A multi-segment concatenated preamble utilizing tagged sequences was developed by [28], simultaneously enhancing frequency offset resilience and large-delay estimation capability. Additionally, dedicated timing offset detection and collision detection algorithms were designed. Based on two LoRa structures, a preamble structure was designed by [29], for which a time offset estimation method was developed to achieve improvements in timing accuracy and expansion of the frequency offset estimation range. [30] similarly incorporated LoRa into the preamble design, with the detection performance of the preamble being analyzed under conditions where timing offsets and frequency offsets were present. A multi-length ZC sequence preamble format was designed by [31], with its symmetrically transmitted properties analyzed and a detection algorithm developed, demonstrating robust performance in the presence of frequency offsets and timing advance (TA). A novel long-preamble sequence structure was architected by [32] through concatenating multiple ZC sequences with differentiated root indices under large-subcarrier-spacing configurations, for which a new timing detection algorithm was devised to estimate Timing Advance (TA), while frequency offset robustness was concurrently demonstrated for the newly designed sequence. A preamble sequence was conceived by [33] through concatenating multiple short-length sequences to extend the Timing Advance (TA) estimation range, with a method devised to achieve accurate TA estimation under adverse conditions of noise and frequency offset presence, while a frequency offset estimation technique was concurrently introduced leveraging the correlation properties of ZC sequences. A paired-root Zadoff-Chu (ZC) sequence approach was employed by [34] for preamble design, wherein the causes of significant estimation errors in frequency offset and Timing Advance (TA) were investigated for conventional paired-root sequences. Based on these findings, a novel root-pairing scheme was proposed, enhancing estimation accuracy.

Reduction of access latency is typically pursued through two principal approaches: collision probability among users is first minimized via optimized allocation and utilization of preamble resources, while random access procedural steps are secondly reduced, with a two-step random access procedure being recognized as a pivotal technology for enabling low-latency communication. Performance

 doi:10.20944/preprints202602.1239.v1

studies conducted by [35] indicate that a RACH procedure founded on a two-message handshake via a specially designed preamble set can achieve latency reduction compared to standard RACH processes, while mathematical analysis of two-step random access performance has been rigorously investigated by [36]. NOMA technology was incorporated by [37] to enhance the two-step random access procedure, with access probability simultaneously optimized through the Access Class Barring (ACB) mechanism, achieving additional access latency reduction via this dual-approach optimization. Building upon latency performance analysis of the two-step random access procedure, a preamble allocation algorithm was proposed by [38] to control latency, thus achieving dual optimization of preamble resource utilization efficiency and latency reduction. Building upon the two-step random access foundation, an enhanced two-step random access scheme for MsgA transmission was further proposed in Literature [39], utilizing many-to-one mapping to elevate resource efficiency, supplemented by a successive interference cancellation (SIC) receiver deployed to decode payloads from distinct users.

Prior to physical random access channel (PRACH) initiation, downlink synchronization is performed primarily to achieve timing and frequency synchronization. When a UAV serves as an aerial node functionally equivalent to a base station, uplink/downlink synchronization between user equipment (UE) and the UAV is directly established, wherein downlink synchronization constitutes device-to-device sidelink communication, specifically classified as sidelink downlink synchronization, whereas current research on sidelink technology remains predominantly focused on terrestrial networks. A joint time-frequency domain synchronization algorithm was developed by [40] incorporating compensation mechanisms for transmission-induced timing offsets and frequency offsets. A link-level simulator was architected by [41] to assess detection performance of C-V2X sidelink SSB (Synchronization Signal Block), incorporating Doppler shift compensation for velocity-induced frequency offsets. A novel Physical Sidelink Broadcast Channel (PSBCH) design was proposed by [42] for millimeter wave (mmWave) systems targeting higher transmission rates, leveraging common-mode signaling to achieve downlink synchronization over mmWave channels.

Research gaps are identified as follows: Uplink synchronization studies predominantly address doppler resilience and coverage extension but assume timing offsets shorter than the symbol duration, leaving multi-symbol offsets underexplored. Compatibility with 5G preamble designs requires resolution. For sidelink downlink synchronization, timing/frequency offsets are critical, but mmWave integration demands further investigation.

3. System Model and Detail Design

The research scenario of this paper is the enhancement of millimeter-wave communication coverage using unmanned aerial vehicles (UAVs), as illustrated in Figure 1. The blue dashed circles represent the communication coverage area of the base station. Outside this area, devices cannot be directly connected to the base station. The black UAVs represent relay UAVs, which communicate directly with the base station. The gray UAVs represent slave UAVs; these UAVs are outside the communication coverage area of the base station and need to first be connected to relay UAVs and then to the base station. In this way, the base station, relay UAVs, and slave UAVs jointly achieve the enhancement of millimeter-wave coverage. Among them, relay UAVs and slave UAVs form a UAV cluster. Different UAV clusters can be dispatched to required locations to provide communication services as needed. As shown in Figure 1, UAV clusters under a same base station can be used for remote sensing, emergency communications and so on. The gray dashed circles represent the extended communication coverage area that the base station can cover through relay UAVs after expansion.

In this scenario, communication is divided into two parts: one part is the communication between the base station and relay UAVs, and the other part is the communication between relay UAVs and slave UAVs. Traditional cellular communication is adopted between the base station and relay UAVs, while sidelink communication is adopted between relay UAVs and slave UAVs. The research content of this paper focuses on the uplink and downlink synchronization issues of the above two communication

 doi:10.20944/preprints202602.1239.v1

parts. The high mobility of UAVs and their wide communication coverage area pose significant challenges to synchronization, which can be summarized into three key issues:

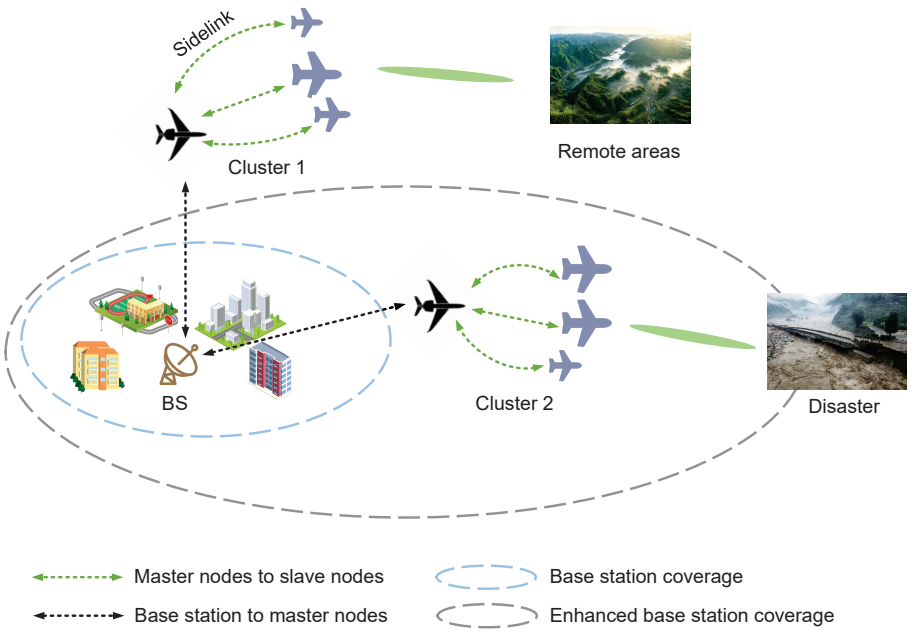

Figure 1. Scenario illustration of highly dynamic UAV swarms for communication coverage extension.

- Problem 1 ($\mathcal{P}1$): UAV Cluster-Relay UAV Uplink Synchronization
  Uplink access for slave UAV faces persistent Doppler interference. Concurrent access attempts from numerous UAVs cause congestion, reducing efficiency and increasing latency. The inherent complexity of four-step RACH procedures further exacerbates delays. Bandwidth allocation requirements per UAV strain spectral resources, demanding resource-efficient, low-latency, Doppler-resilient solutions.
- Problem 2 ($\mathcal{P}2$): Relay UAV-UAV Cluster Downlink Synchronization
  Downlink synchronization via sidelink broadcast channels—originally designed for V2X—exhibits limited Doppler resilience. Current S-SSB designs fail to satisfy UAV frequency offset requirements, necessitating structural and resource reallocation. Resource-efficient utilization must be prioritized given UAV energy constraints, requiring energy-optimized synchronization algorithms and rigorous performance validation.

3.1. Asynchronous NOMA-Based Two-Step Random Access ($\mathcal{P}1$)

3.1.1. Data Structure of 2-Step RACH Based on A-NOMA

5G random access procedure is categorized into two-step and four-step random access based on signaling interactions. The two-step random access reduces interaction rounds between UEs and base stations during connection establishment and resumption, significantly decreasing delay, signaling overhead, and power consumption during random access, thereby improving access efficiency and reducing latency. In the scenario considered herein, the slave UAV is equivalent to UEs, while the relay UAV functions as a base station. Given the constrained onboard energy of UAVs, minimizing power consumption across all communication phases is essential. Consequently, two-step random access is selected for uplink synchronization between relay UAVs and slave UAV.

In two-step random access, the transmission signal combines the preamble and data payload as is illustrated in Figure 2. The preamble is transmitted via PRACH, while the data payload is carried by the PUSCH. These are transmitted sequentially in the time domain, with a guard interval separating the two channels.

 doi:10.20944/preprints202602.1239.v1

Figure 2. Transmission signal structure of two-step rach.

Considering that the frequency resources available to any communication system are limited, maximizing their utilization is imperative, particularly in UAV communications. When a large number of slave UAVs require access, allocating dedicated bandwidth segments to individual UAVs for random access may be infeasible. Furthermore, even two-step random access in traditional OMA systems inevitably encounters congestion and prolonged access delays, resulting in low resource utilization. Therefore, NOMA is introduced into the two-step random access between slave UAVs and relay UAVs. Simultaneously, maintaining perfect synchronization among UAVs during flight is impractical. Thus, a two-step random access procedure integrated with A-NOMA is considered in this work.

Assume the system contains a total of K users. Each user operates at a distinct power level, with power gain magnitudes ordered in descending sequence as $P_1 > P_2 > \cdots > P_K$. Their transmission delays progressively increase $\tau_1 < \tau_2 < \cdots < \tau_K$. These users occupy either fully or partially overlapping bandwidth of B_k. The time-frequency structure of the data is depicted in Figure 3.

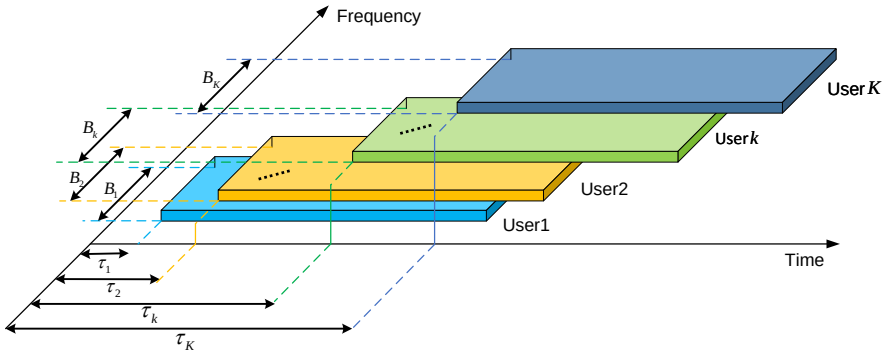

Figure 3. Time-frequency structure of transmission signal.

In UAV communications, two major challenges are posed by high mobility and long transmission distances for A-NOMA:

- Doppler frequency offset: The high velocity of UAVs induces doppler frequency offsets. Existing A-NOMA demodulation schemes are assumed to have known frequency offsets, while mechanisms for frequency offset estimation and compensation are lacking.
- Time delay: Propagation delays cannot be ignored in long-distance transmissions for users. Estimation methods for delays are not studied in existing schemes, which rely on synchronization assumptions.

To address these issues, a preamble structure based on superimposed paired index sequences is proposed during the PRACH transmission phase to achieve joint estimation of frequency offsets and propagation delays. During the PUSCH phase, joint estimation and compensation of frequency offsets are implemented. A detailed description follows.

Assuming the frequency-domain data of the k-th user after constellation mapping is denoted as $S_k[n]$, conversion to the time domain is performed through OFDM modulation as expressed in the formula:

$$s_k[i] = \frac{1}{\sqrt{N}} \sum_{n=0}^{N-1} \sqrt{P_k} S_k[n] e^{j\frac{2\pi in}{N}}, \tag{1}$$

 doi:10.20944/preprints202602.1239.v1

where n represents the n-th subcarrier in the frequency domain, and N denotes the FFT size. A CP is added to this, and symbols are sequentially concatenated to form the complete transmitted signal of the k-th user. The signal received at the receiver after passing through the channel can be expressed as:

$$r[i] = \sum_{k=1}^{K} h_k s_k[i] + w[i], \tag{2}$$

where h_k represents the channel transfer characteristic experienced by the k-th user, and $w[i]$ denotes additive white Gaussian noise with zero mean and variance δ^2. After removing its CP and compensating for time offset, the signal is converted to the frequency domain, with its frequency-domain form given by:

$$\begin{aligned} R[n] &= \frac{1}{\sqrt{N}} \sum_{i=0}^{N-1} r[i + \tau_j + N_{\text{cp}}] e^{-j\frac{2\pi i n}{N}} \\ &= \frac{1}{\sqrt{N}} \sum_{k=j+1}^{K} \sum_{i=0}^{N-1} h_k s_k[i - \Delta\tau_k]^{-j\frac{2\pi i n}{N}} + \sqrt{P_j} H_j S_j[n] + W[n], \end{aligned} \tag{3}$$

where $\Delta\tau_k = \tau_k - \tau_j$, the first part represents interference from users other than user j to user j; the second part denotes the received signal of user j in a noise-free environment; the third part is noise, corresponding to the IFFT of $w[i]$. The interference term can be further expressed as:

$$\eta[n] = \frac{1}{N} \sum_{k=j+1}^{K} \sum_{i=0}^{N-1} \sum_{m=0}^{N-1} \sqrt{P_k} H_k S_k[m] e^{j\frac{2\pi(im - in - \Delta\tau_k m)}{N}}, \tag{4}$$

in case of $m = n$, the interference is mathematically formulated as:

$$\eta[n] = \sum_{k=j+1}^{K} \sqrt{P_k} H_k S_k[n] e^{-j\frac{2\pi\Delta\tau_k n}{N}}, \tag{5}$$

when users are perfectly synchronized, the interference term is given by:

$$\eta[n] = \sum_{k=j+1}^{K} \sqrt{P_k} H_k S_k[n] \tag{6}$$

Taking $K = 2$ as an example, the constellation diagrams for NOMA and A-NOMA are shown in Figure 4. As analyzed in (11) and (12), in the case of 16QAM modulation:

- For synchronous NOMA, the constellation points of two users, each with 16 points, are superimposed, generating a total of 16×16 constellation points.
- For A-NOMA, compared to synchronous NOMA constellations, superimposed constellation points acquire additional phase rotation. This is manifested in the constellation diagram as circular clusters corresponding to the original constellation points of User 1.

 doi:10.20944/preprints202602.1239.v1

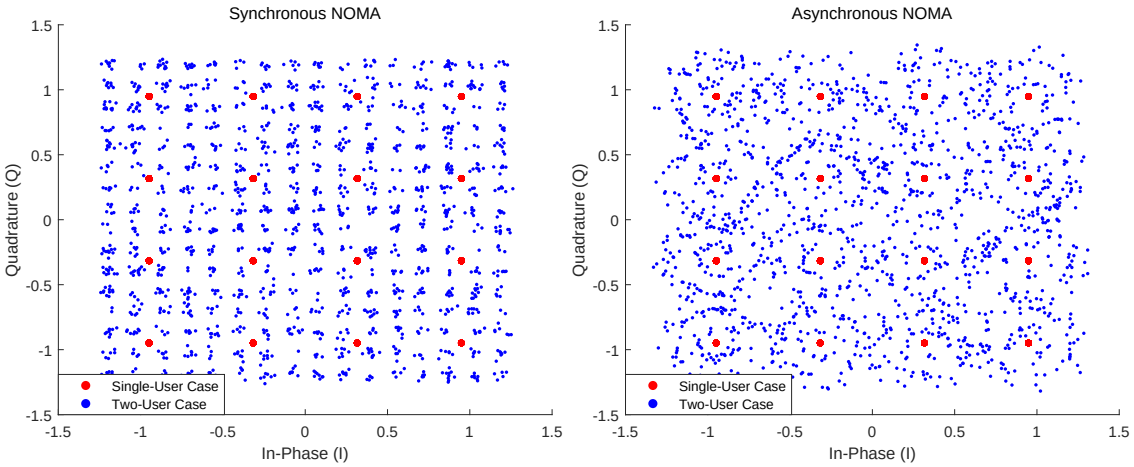

Figure 4. The impact of timing offset.

3.1.2. Impact of Frequency Offsets on A-NOMA

The impact of time asynchrony on NOMA has been introduced, demonstrating that time offset cannot be neglected. The influence of frequency offset on A-NOMA is described below.

With the time of User j serving as the reference, the signal after timing offset (TO) compensation and frequency offset (FO) compensation for User j can be expressed as:

$$R[n] = \frac{1}{N}\sum_{m=0}^{N-1}\sqrt{P_j}h_j S_j[m]\sum_{i=0}^{N-1} e^{-j\frac{2\pi(m-n+\Delta\varepsilon_j)i}{N}} + \xi[n], \tag{7}$$

where $\xi[n] = \eta[n] + W[n]$, The first part of the formula represents the signal of user j. $\Delta\varepsilon_j$ indicating frequency offset estimation error. $\eta[n]$ denotes interference from other users to user j, with detailed derivation provided in Formula (8). Where ε_k represents the frequency offset of the k-th user and $\hat{\varepsilon}_j$ denotes the frequency offset estimate of the j-th user.

$$\begin{aligned}\eta[n] &= \frac{1}{\sqrt{N}}\sum_{k=j+1}^{K}\sum_{i=0}^{N-1} h_k s_k[i-\Delta\tau_k]e^{-j\frac{2\pi in}{N}}e^{j\frac{2\pi(\varepsilon_k(i-\Delta\tau_k)-\hat{\varepsilon}_j i)}{N}} \\ &= \frac{1}{N}\sum_{k=j+1}^{K} e^{-j\frac{2\pi\varepsilon_k\Delta\tau_k}{N}}\sum_{m=0}^{N-1}\left[\sqrt{P_k}H_k S_k[m]e^{-j\frac{2\pi\Delta\tau_k m}{N}}\sum_{i=0}^{N-1} e^{j\frac{2\pi i(\varepsilon_k-\hat{\varepsilon}_j+m-n)}{N}}\right]\end{aligned} \tag{8}$$

If the frequency deviation between other users and user j is an integer multiple of the carrier frequency, the interference can be written as:

$$\eta[n] = \sum_{k=j+1}^{K}\sqrt{P_k}H_k S_k[n-(\varepsilon_k-\hat{\varepsilon}_j)]e^{-j\frac{2\pi\Delta\tau_k(n+\varepsilon_k)}{N}} \tag{9}$$

If the difference is a fractional multiple of the carrier FO, the interference can be expressed by (10). For example, with $K = 2$, the above equations (9)-(10) and Figure 5 show that:

 doi:10.20944/preprints202602.1239.v1

$$\begin{aligned}\eta[n] &= \frac{1}{N}\sum_{k=j+1}^{K} e^{-j\frac{2\pi\varepsilon_k\Delta\tau_k}{N}} \sum_{m=0}^{N-1}\left[\sqrt{P_k}H_kS_k[m]e^{-j\frac{2\pi\Delta\tau_k m}{N}}\sum_{i=0}^{N-1}e^{j\frac{2\pi i(\varepsilon_k-\hat{\varepsilon}_j+m-n)}{N}}\right] \\ &= \sum_{k=j+1}^{K}\left[\sqrt{P_k}H_kS_k[n]e^{-j\frac{2\pi\Delta\tau_k(n+\varepsilon_k)}{N}}\frac{\sin\pi(\varepsilon_k-\hat{\varepsilon}_j)}{N\sin(\pi(\varepsilon_k-\hat{\varepsilon}_j)/N)}e^{j\frac{\pi(\varepsilon_k-\hat{\varepsilon}_j)(N-1)}{N}}\right. \\ &+ \left.\sum_{m=0,m\neq n}^{N-1}\sqrt{P_k}H_kS_k[m]e^{-j\frac{2\pi\Delta\tau_k(m+\varepsilon_k)}{N}}e^{j\frac{\pi(m-n)(N-1)}{N}}\frac{\sin\pi(\varepsilon_k-\hat{\varepsilon}_j+m-n)}{N\sin(\pi(\varepsilon_k-\hat{\varepsilon}_j+m-n)/N)}e^{j\frac{\pi(\varepsilon_k-\hat{\varepsilon}_j)(N-1)}{N}}\right]\end{aligned} \tag{10}$$

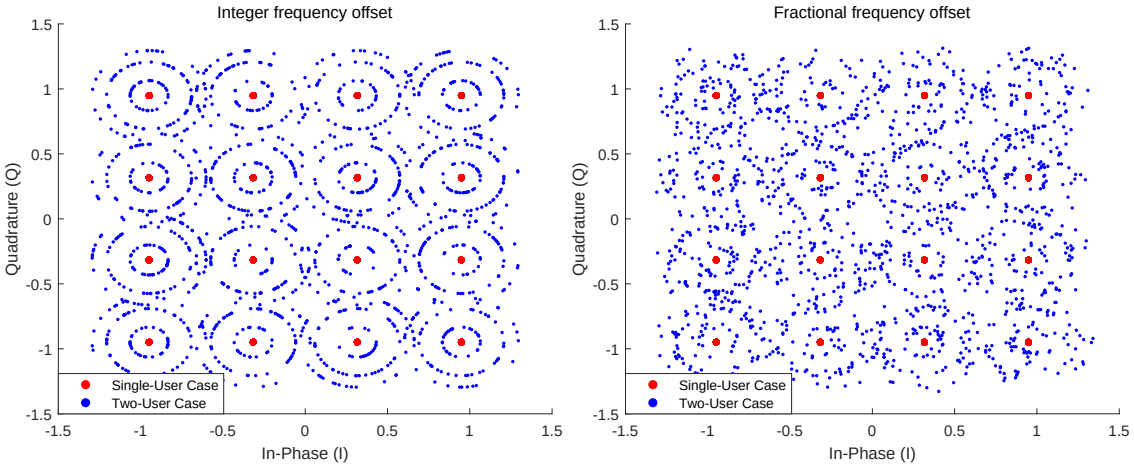

Figure 5. The impact of frequency offset.

- When the FO of User 2 and the estimated FO of User 1 differ by an integer multiple of the FO, interference from User 2 induces both a frequency discrepancy and phase misalignment in User 1, causing phase rotation in the constellation diagram.
- When the FO difference is fractional: The first term shows amplitude and phase distortion in the in the interfering subcarrier components. The second term indicates that the m-th subcarrier suffers interference from other subcarriers, breaking orthogonality.

3.2. Offset Estimation and Reception Procedure

3.2.1. Design of PRACH Paired Sequence

The preamble utilizes ZC sequences, known for their correlation properties, with the mathematical expression:

$$x_u[n] = e^{-j\pi\frac{un(n+1)}{N_{ZC}}}, \quad 0 \le n \le N_{ZC}-1, \tag{11}$$

where u is the root index and N_{ZC} the sequence length, with normalized frequency offset Δf (relative to subcarrier spacing), a time delay τ and Δf during transmission yield the received preamble:

$$y[n] = hx_u[n-\tau]e^{\frac{j2\pi n\Delta f}{N_{ZC}}} + w[n], 0 \le n \le N_{ZC}-1 \tag{12}$$

 doi:10.20944/preprints202602.1239.v1

At the receiver, correlation computation of the ZC sequence is performed to determine both the root index and cyclic shift amount, and can be expressed as:

$$\begin{aligned} R_u[m] &= \sum_{n=0}^{N_{ZC}-1} y[n] x_u^*[n+m] \\ &= h e^{j\varphi[m]} \sum_{n=0}^{N_{ZC}-1} e^{\frac{j2\pi n}{N_{ZC}}(u\tau+um+\Delta f)} + \mathcal{W}[n], \end{aligned} \tag{13}$$

where $\varphi[m] = \pi(m+\tau)(m-\tau+1)/N_{ZC}$, the correlation result can be further expressed as:

$$|R_u[m]| = |h| \left| \frac{\sin \pi(\Delta f + u(m+\tau))}{\sin \pi(\Delta f + u(m+\tau))/N_{ZC}} \right| \tag{14}$$

The preceding equation confirms that frequency FO and TO jointly determine the correlation modulus magnitude. Deviation beyond tolerance thresholds displaces the correlation peak, causing direct degradation of access performance. Current PRACH preambles address simultaneous FO/TO estimation through superimposed sequences with differing root indices u_1 and u_2.

Let e_{u_1} and e_{u_2} denote the preamble sequences generated from root indices u_1 and u_2, with applied cyclic shifts of $v_1 \cdot N_{cs}$ and $v_2 \cdot N_{cs}$, respectively, $e_{u_1} = x_{u_1}[(n + v_1 N_{CS}) \bmod N_{ZC}]$, $e_{u_2} = x_{u_2}[(n + v_2 N_{CS}) \bmod N_{ZC}]$. The received signal at the receiver can be expressed as:

$$y[n] = \sum_{k=1}^{2} x_{u_k}[(n + v_k N_{CS} - \tau) \bmod N_{ZC}] e^{\frac{j2\pi n \Delta f}{N_{ZC}}}, \tag{15}$$

here N_{CS} specifies the cyclic shift interval. The receiver performs correlation, and for u_1, the expression is:

$$\begin{aligned} R[m] &= \sum_{n=0}^{N_{ZC}-1} y[n] x_{u_1}^*[n+m] \\ &= h(R_{u_1,u_1}[m] + R_{u_2,u_1}[m]) + \mathcal{W}[n], \end{aligned} \tag{16}$$

$R_{u_1,u_1}[m]$ is mathematically defined as follows:

$$R_{u_1,u_1}[m] = e^{j\xi[m]} \left(\sum_{n=0}^{N_{ZC}-1} e^{\frac{j2\pi n}{N_{ZC}}(\Delta f - u_1(v_1 N_{CS} - m - \tau))} \right) \tag{17}$$

Given $\xi[m] = m^2 + m - v_1^2 N_{CS}^2 + 2\tau v_1 N_{CS} - \tau^2 - v_1 N_{CS} + \tau$ and distinct root indices between sequences, cross-correlation is negligible relative to auto-correlation. Consequently, the correlation output is dominated by the auto-correlation term, yielding the peak position:

$$\begin{cases} m_1 = (v_1 N_{CS} - \tau - \frac{\Delta f}{u_1}) \bmod N_{ZC} \\ m_2 = (v_2 N_{CS} - \tau - \frac{\Delta f}{u_2}) \bmod N_{ZC} \end{cases} \tag{18}$$

Under conditions $v_1 = v_2$ and $u_1 + u_2 = N_{ZC}$, the preambles for u_1 and u_2 exhibit complex conjugation. Therefore, FO and TO estimates follow:

$$\begin{cases} \hat{\tau} = \frac{1}{2}[-(m_1 + m_2)] \bmod N_{ZC} \\ \Delta\hat{f} = \frac{u_1}{2}[-(m_1 - m_2)] \bmod N_{ZC} \end{cases} \tag{19}$$

 doi:10.20944/preprints202602.1239.v1

3.2.2. Complexity Analysis

For the frequency offset and time offset estimation algorithm mentioned earlier, its specific implementation process can be divided into three key steps: First, the receiver captures the preamble signal. Due to the inevitable time offset and frequency offset interference during the transmission process, the finally obtained signal is a preamble time-domain sequence with deviations; Second, since the generation rule of the preamble is preset and known, the receiver can pre-construct the preamble reference signal, which belongs to the category of frequency-domain signals and has not been processed by IFFT; Finally, the receiver performs an IFFT transformation on the pre-constructed reference sequence to convert it from the frequency domain to the time domain, and then uses the detection algorithm described earlier to complete the accurate estimation of time offset and frequency offset. When adopting this implementation method, the computational complexity of the algorithm is mainly composed of two parts: one is the computational complexity caused by the IFFT transformation, whose order of magnitude is $\mathcal{O}(N \log N)$; the other is the complexity brought by the time-domain correlation operation, corresponding to the order of magnitude of $\mathcal{O}(N^2)$. Overall, the total complexity of the algorithm is $\mathcal{O}(N^2)$. The total complexity of the algorithm is derived as follows:

$$\mathcal{O}(N \log N) + \mathcal{O}(N^2) \approx \mathcal{O}(N^2) \tag{20}$$

From the perspective of the inherent mathematical relationship between cross-correlation and convolution, the cross-correlation operation between two sequences can be converted into the convolution operation of one sequence and the other sequence after time-domain inversion processing. Combined with the convolution theorem in Fourier transform, the convolution operation at the time-domain level can be further converted into the multiplication operation at the frequency-domain level, and its corresponding mathematical expression is shown as follows:

$$R_{xy}[m] \rightarrow X(f) * Y(f) \tag{21}$$

In the above formula, R_{xy} represents the cross-correlation operation result of the two sequences, and $*$ denotes the convolution operation symbol. Through the above operation conversion, the complexity of the correlation operation is significantly optimized, reducing from $\mathcal{O}(N^2)$ of the original time-domain operation to $\mathcal{O}(N)$ of the frequency-domain multiplication operation. In the algorithm designed in this paper, the detection process of FO and TO needs to be completed in the time domain relying on paired preamble sequences. Based on this, it is necessary to convert the result of the frequency-domain correlation operation back to the time domain through IFFT operation, and the computational complexity generated by this inverse conversion process is $\mathcal{O}(N \log N)$. It should be specially noted that in the detection process of the preamble sequence, converting the received signal to the frequency domain is an indispensable basic preprocessing step, and the computational load of this step is not included in the statistical scope of the algorithm complexity. Based on the above analysis, the overall complexity of the algorithm is equal to the sum of the frequency-domain correlation operation complexity and the IFFT inverse conversion operation complexity, and the specific calculation formula is as follows:

$$\mathcal{O}(N \log N) + \mathcal{O}(N) \approx \mathcal{O}(N \log N) \tag{22}$$

3.2.3. Procedure for A-NOMA Based Two-Step Random Access

This section establishes the receiving process of two-step random access based on a-NOMA, as shown in Figure 6. The received signal undergoes preamble detection to determine which users are included. During this process, the power of each detected preamble sequence can be obtained to distinguish them. Then, the above estimation method is used to estimate the frequency offset and time offset. After the frequency offset and time offset of one user are detected, that user is subtracted from the received preamble, and the detection of the frequency offset and time offset of the next user

 doi:10.20944/preprints202602.1239.v1

continues until the time offsets and frequency offsets of all users are detected. Next, starting from the first user, the frequency offset and time offset of its PUSCH are compensated, and then the decoding process of PUSCH is completed. Similarly, the PUSCH data of that user is subtracted before decoding the next user, with the processing order following the descending order of power.

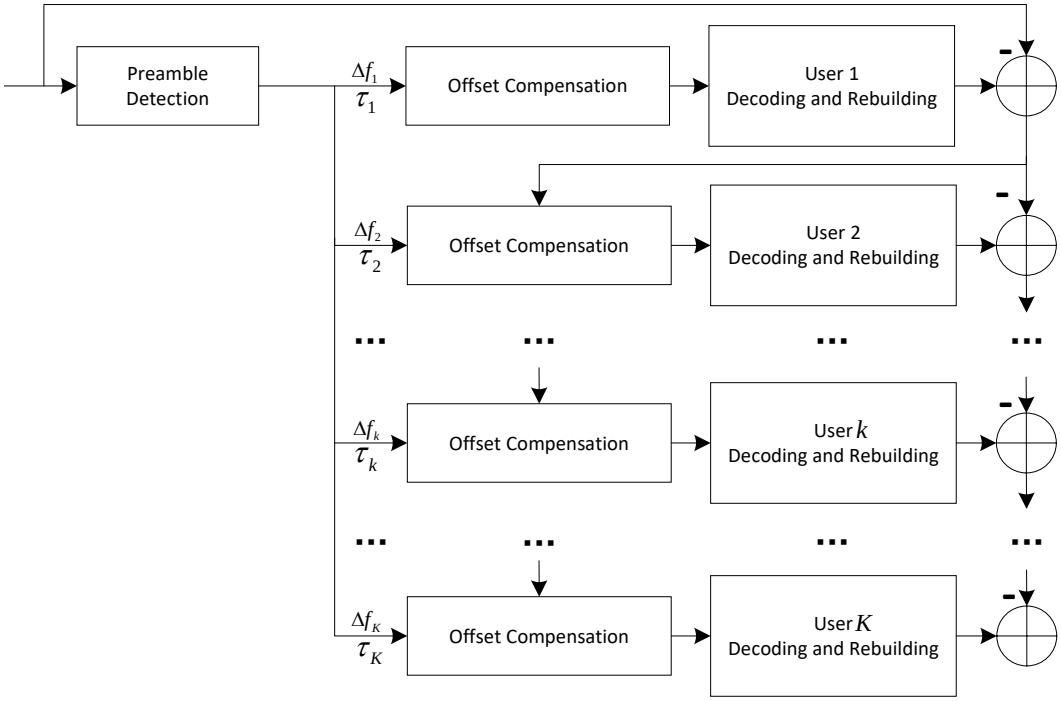

Figure 6. Reception procedure.

3.3. Downlink Synchronization for Millimeter-wave Based Sidelink (P2)

Four dedicated physical channels are utilized by sidelink for synchronization, data transmission, and control functions. Among these channels, downlink synchronization is facilitated by the physical sidelink broadcast channel (PSBCH). S-SSB is periodically broadcast by the base station, and they are received and demodulated by User Equipments (UEs) to complete downlink synchronization. Each S-SSB is loaded with synchronization signals, demodulation reference signals (DM-RS), and payload data.

In the frequency domain, 11 resource blocks (RBs) are occupied by the S-SSB. In the time domain, two CP formats are employed for different coverage scenarios, namely normal CP and extended CP; these two formats correspond to 12 and 14 orthogonal frequency-division multiplexing (OFDM) symbols, respectively. The synchronization signals consist of a S-PSS and a S-SSS. Unlike the SSB in cellular communication, two OFDM symbols are allocated to each of these two signals—a design by which synchronization detection performance is significantly enhanced. Symbols 2 and 3 are fixed for the S-PSS, while symbols 4 and 5 are occupied by the S-SSS. DM-RS is embedded in all symbols except those in which synchronization signals are carried; one DM-RS resource element (RE) is allocated for every four REs, so that a frequency-domain density of one-quarter is achieved. All remaining resources are dedicated to payload transmission.

The S-PSS and S-SSS are generated from an m-sequence and a Gold sequence, respectively. Both sequences have a length of 127, and 127 subcarriers in the frequency domain are occupied by each of them. The generation of synchronization signals is linked to two SideLink Identifiers (SLIDs), which jointly form the user identifier (ID). Through this design, the differentiation of up to 672 distinct users is enabled.

 doi:10.20944/preprints202602.1239.v1

The redesigned S-SSB for downlink synchronization between slave UAVs and relay UAVs is presented in this paper, accompanied by a complete simulation framework where computational complexity, doppler shifts, and timing offsets are comprehensively incorporated.

As illustrated in Figure 7, in this design, only the extended CP is retained. This modification is implemented to simultaneously enhance coverage and increase payload capacity, with the acknowledgment that latency sensitivity is reduced in wide-coverage aerial scenarios.

In the frequency domain, the standard allocation of 11 RBs is expanded to 24 RBs. This expansion is driven by the dual objectives of augmenting payload capacity and enhancing communication coverage. Crucially, the primary impact on performance is attributed to the redesign of signals within the resource blocks rather than the scaling of bandwidth itself.

The signal components—S-PSS, S-SSS, DM-RS, and payload—are retained but with structural adjustments. The S-PSS and S-SSS preserve their standard S-SSB configuration: S-PSS occupies symbols #1 – #2 and S-SSS occupies symbols #3 – #4, with no alterations to sequence generation or resource mapping.

For DM-RS, three key modifications are introduced:

- The conventional approach of scattered distribution across all non-synchronization symbols is replaced with three concentrated double-symbol DM-RS groups, which occupy a total of 6 symbols. The purpose of this modification is to minimize DM-RS resource occupation and improve capacity, while preventing the failure of channel estimation and frequency offset estimation in rapidly varying channels affected by Doppler frequency shifts.
- The frequency-domain density of DM-RS is increased from 25% (1 DM-RS RE corresponding to every 4 REs) to 50% (1 DM-RS RE corresponding to every 2 REs). This adjustment aims to track rapid channel variations, optimize the relationship between demodulation performance and resource occupation through symbol-level sparse insertion, and improve the accuracy of channel estimation and frequency offset estimation.
- The first DM-RS group is multiplexed with the S-PSS in symbols #1–#2: the two share the symbol duration while occupying different frequency resources, which serves to improve the accuracy of channel estimation.

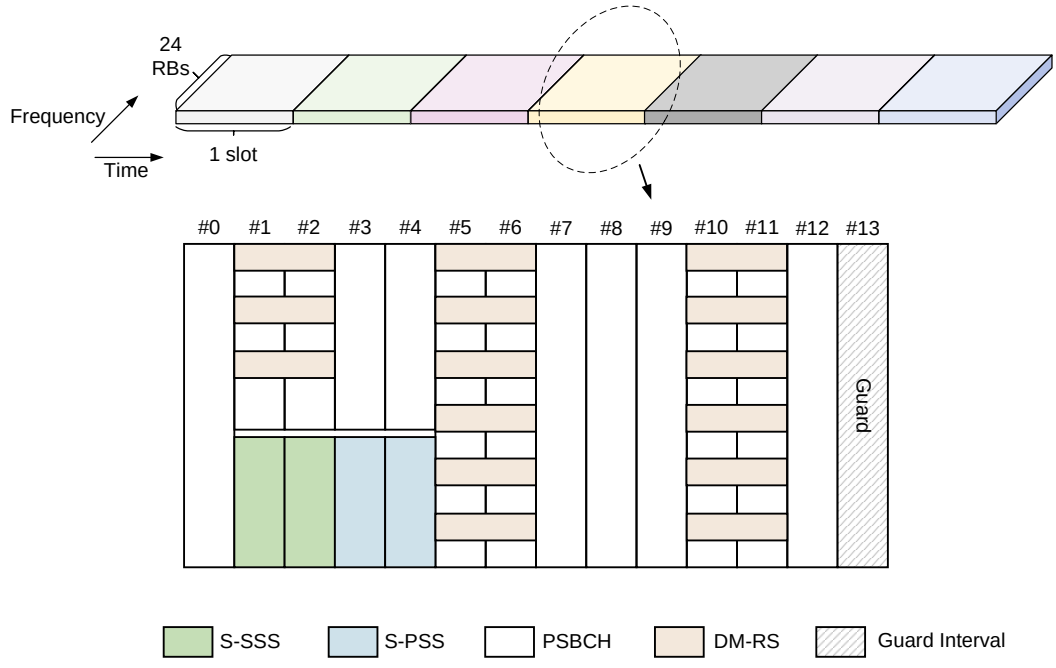

Figure 7. New structure of S-SSB.

 doi:10.20944/preprints202602.1239.v1

3.3.1. Implementation of Signal Generation and Reception Algorithms

The generation of the S-SSB refers to the creation of transmitted signals carried within the S-SSB. The generation procedures for S-PSS, S-SSS, and DM-RS remain identical to those in the original S-SSB, with the sole distinction being the quantity of DM-RS.

The data transmission process is executed through the following steps:

- CRC Attachment: A 24-bit Cyclic Redundancy Check (CRC) is attached to the payload.
- Channel Coding: Low-density parity-check (LDPC) coding is selected due to its suitability for large data blocks and high-throughput transmission in system synchronization channels.
- Rate Matching: Rate matching is applied to the encoded blocks.
- Concatenation: The rate-matched blocks are concatenated.
- Scrambling: The concatenated blocks are scrambled.
- Modulation: The scrambled blocks are modulated using quadrature phase-shift keying (QPSK).
- Resource Mapping & Transmission: The synchronization signals (S-PSS/S-SSS), DM-RS, and payload are mapped to their designated positions within the synchronization block and subsequently transmitted.

A signal demodulation algorithm for the redesigned S-SSB is proposed, as illustrated in Figure 8. To reduce computational load, down-sampling-based S-PSS detection is employed during the S-PSS detection stage, where time offset estimation is divided into coarse estimation and fine estimation. Subsequent procedures include S-SSS detection, channel estimation, TA estimation and compensation, FO estimation and compensation, channel equalization, and decoding.

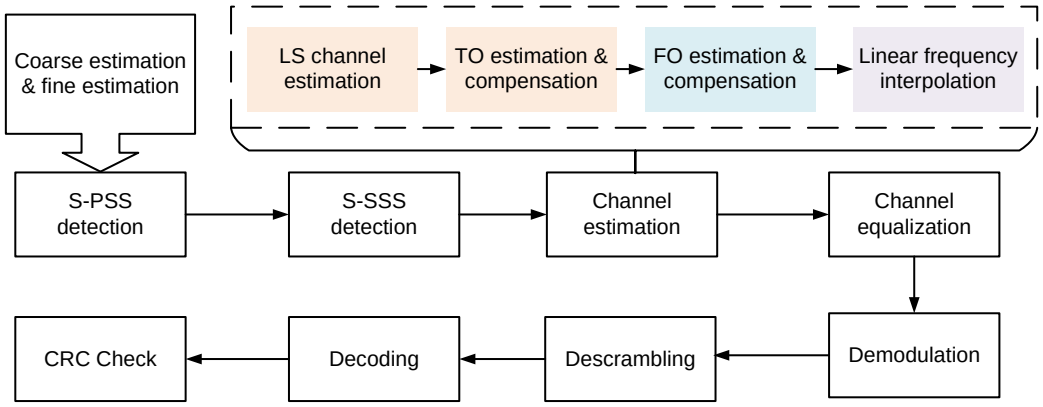

Figure 8. S-SSB reception procedure.

The primary objective of S-PSS detection is defined as identifying SL-ID2 and the timing offset incurred during transmission. S-PSS signal detection is performed in the time domain. Since S-PSS signal generation is solely dependent on SL-ID2 and the generation method is known to both communication parties, the receiver traverses all possible values of SL-ID2 to generate corresponding S-PSS sequences. Following the identical processing flow as the transmitter, an S-SSB resource block containing only the S-PSS signal is generated, modulated via OFDM, and converted to the time domain. This signal is then correlated with the received signal to obtain correlation results for each SL-ID2. Among results exceeding a predefined threshold, the SL-ID corresponding to the S-PSS with the highest correlation peak is identified as the transmitted value, while the peak position offset is interpreted as the timing offset.

Conventional S-PSS detection relies on direct time-domain correlation of two signals. Given the typically long sequence lengths, this approach incurs substantial computational load. In UAV applications, where on-board energy is constrained, computational efficiency must be prioritized for energy conservation. Consequently, the timing offset estimation is partitioned into coarse and fine estimation stages. The receiver similarly generates the S-SSB and converts it to the time domain but applies an a fold downsampling to both signals before correlation. The resulting downsampled

 doi:10.20944/preprints202602.1239.v1

correlation represents an a fold decimated version of the original correlation output. While this reduces computation, the downsampled correlation peak may not align with the original peak. Thus, fine estimation is required to determine the precise timing offset.

Within ±1 sample of the downsampled correlation peak, the original correlation peak must lie within $\pm a$ samples of the coarse estimate position. By extracting $\pm a$ samples around the coarse estimate from the original signals and performing correlation, the exact timing offset is obtained.

S-SSS detection serves to determine SL-ID1. After timing offset compensation via S-PSS detection, the received signal is transformed to the frequency domain via FFT, from which the received S-SSS is extracted. S-SSS detection employs frequency-domain correlation to minimize computation. The S-SSS is determined jointly by SL-ID1 and SL-ID2. With SL-ID2 identified through S-PSS detection, all possible SL-ID1 values are traversed to generate corresponding S-SSS sequences. These sequences are correlated with the received signal, and the S-SSS yielding the highest correlation peak is selected as the correct sequence.

Channel estimation utilizes DM-RS within PSBCH, proceeding through:

- Least-squares (LS) channel estimation
- Timing offset estimation and compensation
- Frequency offset estimation and compensation
- Linear frequency interpolation

The channel response is derived after these steps. Finally, equalization is performed based on the Minimum Mean Square Error (MMSE) criterion. Payload demapping and decoding follow the inverse procedure of the transmission chain.

4. Simulation Results

4.1. Simulation and Performance Discussion for $\mathcal{P}1$

For asynchronous NOMA random access, this section presents the simulation results of PRACH and PUSCH under the scenarios of two users and three users, as well as the impact of frequency offset and time offset on the demodulation of both. It also studies the influence of different frequency-domain overlaps among different users on the demodulation of PUSCH. The simulation configurations are shown in Table 1.

Table 1. Simulation parameters ($K = 2$).

Parameters	Value
Channel	AWGN
Power ratio	15 : 1
System subcarrier spacing (KHz)	60
Timing offset (sample)	0 / 650
Frequency offset (KHz)	0 / 13
Bandwidth (MHz)	100

The power ratio of the two users is 15 : 1, with millimeter-wave transmission adopted and a subcarrier spacing of 60 KHz. The TO of arrival between the two users is 650 samples, corresponding to an actual distance of approximately 800 meters, and the Doppler frequency offset is 13 KHz. The core reason for selecting a 13 KHz Doppler frequency offset is to fit the characteristics of millimeter-wave transmission. At a typical millimeter-wave carrier frequency (e.g., 28 GHz), according to the Doppler frequency offset calculation formula $f_d = \frac{v \cdot f_c}{c}$ (where v is the moving speed, f_c is the carrier frequency, and c is the speed of light), a 13 KHz frequency offset corresponds to a conventional moving speed of about 46 km/h for users in short-to-medium distance communication (such as UAV and vehicle-mounted scenarios). This moving speed is consistent with the actual application of such scenarios, making the value reasonable; at the same time, this frequency offset has a clear and reasonable matching relationship with the 60 KHz subcarrier spacing. After calculation, the proportion

 doi:10.20944/preprints202602.1239.v1

of 13 KHz to the 60 KHz subcarrier spacing is about 21.7%. This proportion can not only reflect the impact of frequency offset on the system, but also effectively verify the accuracy and performance of the designed frequency offset estimation algorithm.

Figure 9 illustrates the effects of different frequency offsets and timing offsets on PRACH detection in the two-user scenario. Specifically, TO1 and TO2 denote the timing offsets of the first and second users relative to the slot boundary at the receiver respectively. the arrival time of User 2 is 650 samples later than that of User 1. It is shown by the simulations that the impact of frequency offset on the performance of User 1 is far smaller than that on User 2. This is consistent with the derivation in (14), which states that frequency offset affects PRACH detection performance by influencing the magnitude of the correlation operation's modulus. In this case, since the power of User 1 is amplified by 15 times, the frequency offset is insufficient to affect the correlation result; thus, the performance of User 1 is not impacted by frequency offset. This indicates that frequency offset in PRACH can be mitigated through power amplification. Furthermore, by comparing the PRACH detection performance under synchronous (no TO difference) and asynchronous (with TO difference) conditions between User 2 and User 1, it is found that appropriate asynchrony exerts a positive effect on PRACH detection and helps improve detection performance.

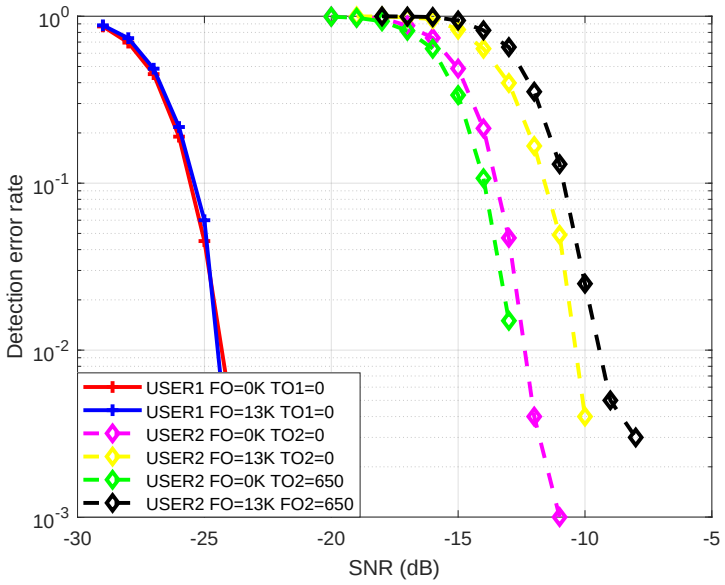

Figure 9. Detection performance of PRACH ($K = 2$).

Figure 10 and 11 respectively demonstrate the PUSCH demodulation performance of different users employing QPSK and 16QAM modulation schemes, under the aforementioned frequency offset and TO conditions. As can be observed from the figure, both TO and FO significantly degrade the PUSCH demodulation performance. When considering the impact of TO alone, there is a noticeable difference in PUSCH demodulation performance between TO = 120 samples and TO = 650 samples: PUSCH demodulation performance is improved when TO = 120 samples, while it is significantly degraded when TO = 650 samples. This confirms the aforementioned conclusion that moderate asynchrony can enhance demodulation performance. Moreover, PRACH exhibits greater resilience to asynchrony than PUSCH, which may be attributed to the fact that PRACH detection involves simpler operations compared to PUSCH demodulation, and asynchrony reduces the probability of false correlation between the two sequences.

 doi:10.20944/preprints202602.1239.v1

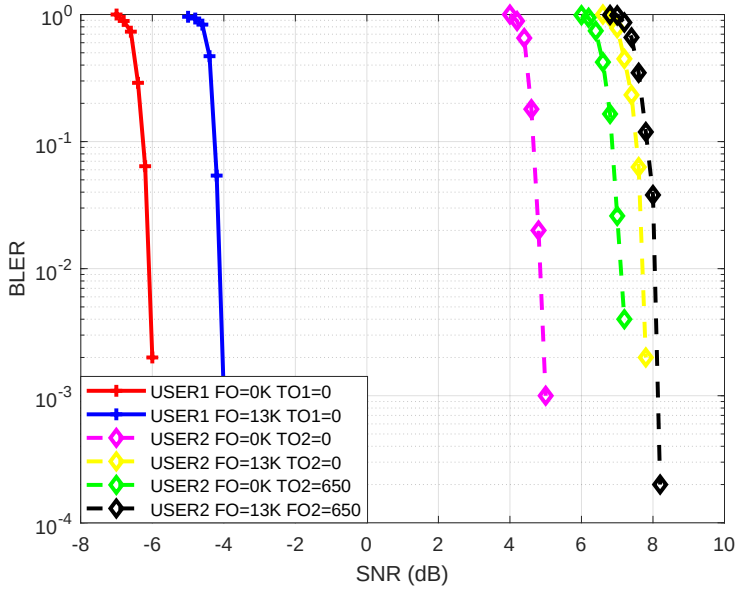

Figure 10. Detection performance of PRACH (QPSK, $K = 2$).

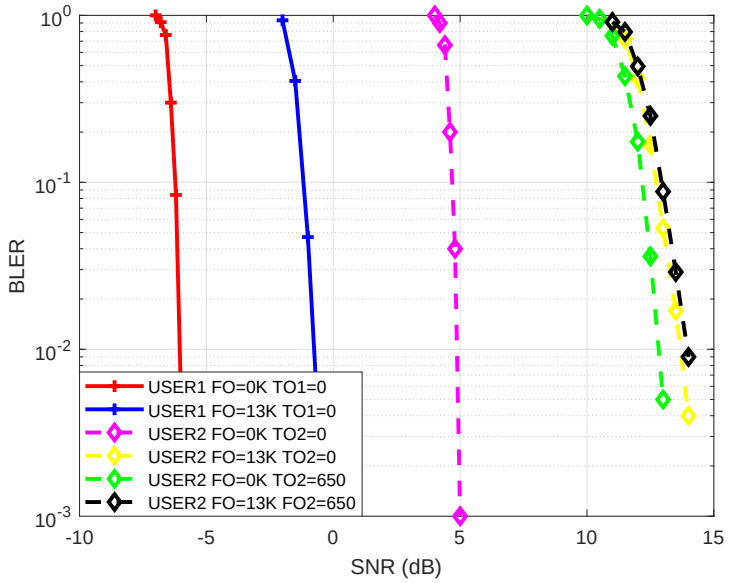

Figure 11. Demodulation performance of PUSCH (16QAM, $K = 2$).

NOMA requires different users to share the same frequency resources, so the bandwidths of different users are completely overlapping. It is worth studying whether partial overlap will affect the demodulation performance. To address this issue, a frequency overlap factor is proposed, defined as in the formula:

$$\beta = \begin{cases} B_o / B_1 (B_1 = B_2) \\ B_o / \min(B_1, B_2) (B_1 \neq B_2) \end{cases} \tag{23}$$

where, B_1 and B_2 represent the bandwidths of User 1 and User 2, respectively. If two users occupy exactly the same bandwidth, β is the ratio of the overlapping part to the bandwidth; if the two users have different bandwidths, β is the ratio of the overlapping part to the bandwidth of the user with the narrower bandwidth.

Figure 12 shows the demodulation performance of PUSCH under the conditions of 0%, 50%, 75%, and 100% overlap ratios. It can be observed that the less the frequency-domain overlap, the better the

 doi:10.20944/preprints202602.1239.v1

demodulation performance. This is expected to provide guidance for resource allocation, such as the joint optimization of time and frequency.

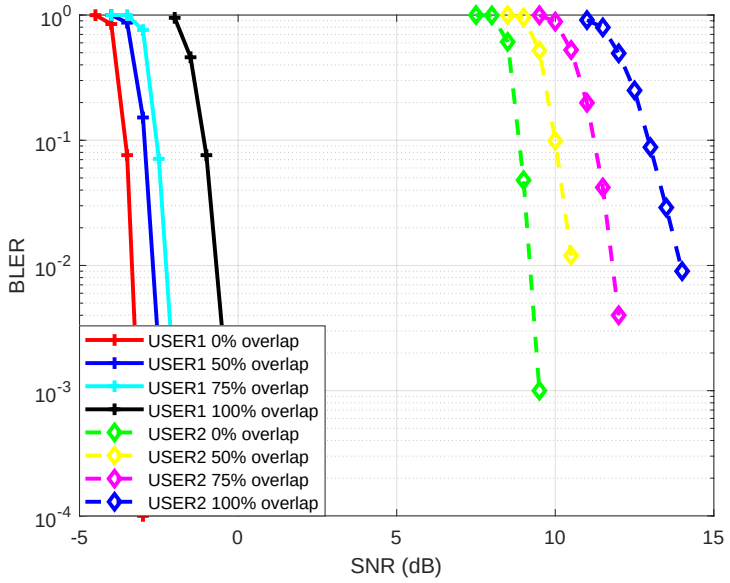

Figure 12. The impact of β on the performance of PUSCH demodulation ($K = 2$).

To verify the universality of the algorithm with respect to the number of users, simulations were conducted for the three-user scenario. The specific configurations are shown in Table 2. Through simulation experiments, it is found that the FO tolerance in the three-user case decreases; therefore, the FO here is no longer set to 13 KHz but adjusted to 5 KHz, which accounts for approximately 8.33% of the 60 KHz subcarrier spacing. For the same reason, the power ratio among users was also modified, and the power ratio of the three users was set to 200 : 20 : 5, while the remaining configurations remain unchanged.

Table 2. Simulation parameters ($K = 3$).

Parameters	Value
Channel	AWGN
Power ratio	200 : 20 : 5
System subcarrier spacing (KHz)	60
Timing offset (sample)	0 / 144 / 180
Frequency offset (KHz)	0 / 5
Bandwidth (MHz)	100

The PRACH detection performance of the three users under different FO and TO conditions is presented in Figure 13. It can be observed that relatively small performance variations are exhibited by User 1 under certain TO and FO conditions; similarly, the influence of 5 KHz FO and a certain time delay has little impact on User 2. In contrast, significant performance differences are shown by User 3 under the aforementioned conditions. Additionally, the performance differences among the three users are consistent with the general understanding of NOMA.

 doi:10.20944/preprints202602.1239.v1

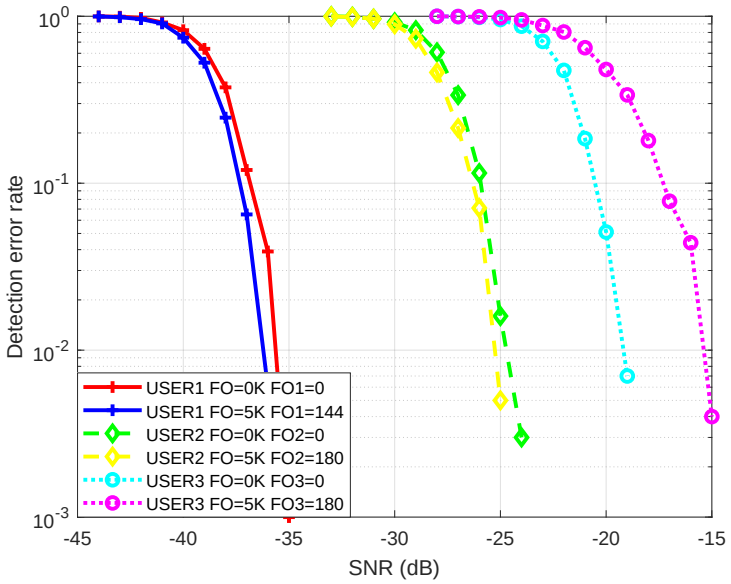

Figure 13. Detection performance of PRACH ($K = 3$).

The PUSCH demodulation performance of the three users under different frequency offset (FO) and timing offset (TO) conditions is presented in Figure 14 and 15, where Figure 14 corresponds to the QPSK modulation scheme and Figure 15 corresponds to the 16QAM modulation scheme. Very limited impact on User 1 is exerted by the applied FO and TO, while relatively significant effects on the data demodulation of Users 2 and 3 are exerted by the same FO and TO. It can be observed that a significant decrease in the performance of Users 2 and 3 is caused after TO and FO are applied—for User 3 in particular, extreme difficulty in data demodulation is encountered. This is the reason why the FO was set to 5 KHz in the three-user simulation, as this FO is already close to the tolerance limit.

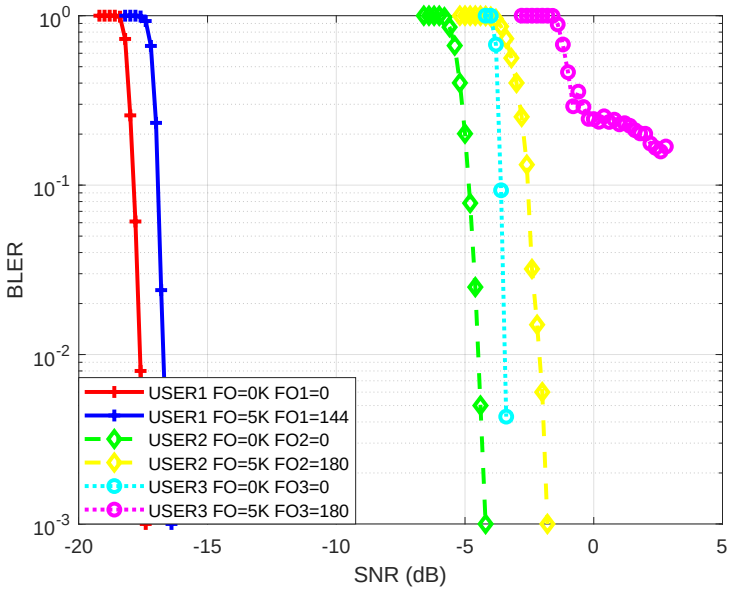

Figure 14. Demodulation performance of PUSCH (QPSK, $K = 3$).

 doi:10.20944/preprints202602.1239.v1

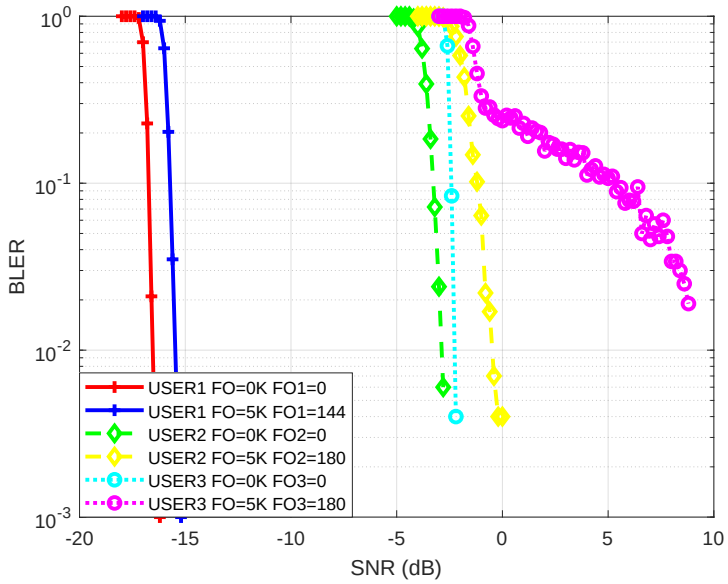

Figure 15. Demodulation performance of PUSCH (16QAM, $K = 3$).

The impact of different frequency-domain overlaps on data demodulation is presented in Figure 16. To control variables, FO and TO were not applied in this case. Among the parameters, β_{12} is defined as the overlap ratio between User 1 and User 2, and β_{23} is defined as the overlap ratio between User 2 and User 3. As shown in the figure, for User 1, better demodulation performance is achieved when the overlap ratio is lower and the number of users overlapping with it is smaller. This conclusion is also applicable to User 2. Notably, this conclusion is not followed by User 3; this is possibly because a greater impact on its performance is caused by its lower power than by frequency-domain overlap.

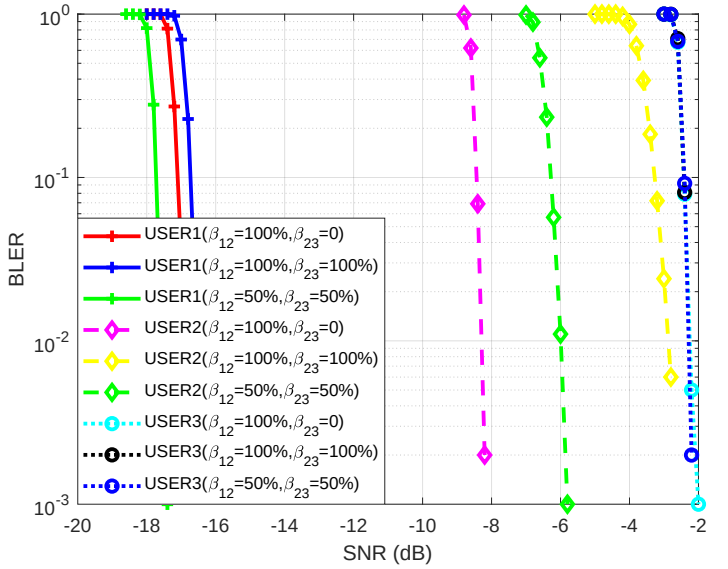

Figure 16. The impact of β on the performance of PUSCH demodulation ($K = 3$).

The conclusions obtained in the three-user scenario are basically consistent with those obtained in the two-user scenario, which demonstrates the feasibility of the scheme. However, it can be observed that the tolerance to frequency offset and asynchrony is found to decrease as the number of users increases.

 doi:10.20944/preprints202602.1239.v1

4.2. Simulation and Performance Discussion for $\mathcal{P}2$

Simulation analysis of the sidelink downlink synchronization channel design is performed with parameters specified in Table 3.

Table 3. Simulation parameters.

Parameters	Value
Channel	AWGN
System subcarrier spacing (KHz)	60
Down-sampling	4× / 8× / 16×
Bandwidth (MHz)	200
Frequency offset (KHz)	0 / 11

The AWGN channel is employed, and the system subcarrier spacing is set to 60 KHz. To minimize link complexity as much as possible, a downsampling method is adopted during S-PSS detection. Simulation evaluations are conducted for downsampling factors of 4×, 8×, and 16× respectively, with frequency offsets of 0 KHz and 11 KHz, which accounts for approximately 18.33% of the 60 KHz subcarrier spacing. The rationale for adopting 11 KHz instead of 13 KHz in this simulation scenario is that experimental tests have demonstrated that under the condition of 8× downsampling, the frequency offset of 13 KHz fails to achieve complete data demodulation. Consequently, 11 KHz is selected as the frequency offset to effectively exhibit the practical performance of the downsampling method employed in S-PSS detection.

The detection performance of S-PSS under different downsampling factors and frequency offsets is presented in Figure 17. It can be observed from the figure that the degradation of S-PSS detection performance caused by downsampling is far more significant than that caused by frequency offsets; as the downsampling factor increases, the detection performance degrades accordingly. Although downsampling is only applied during the S-PSS detection phase, the detection performance of S-SSS and SLID also degrades because their detection is dependent on results of S-PSS, exhibiting a variation trend similar to that of S-PSS detection, as presented in Figure 18 and Figure 19.

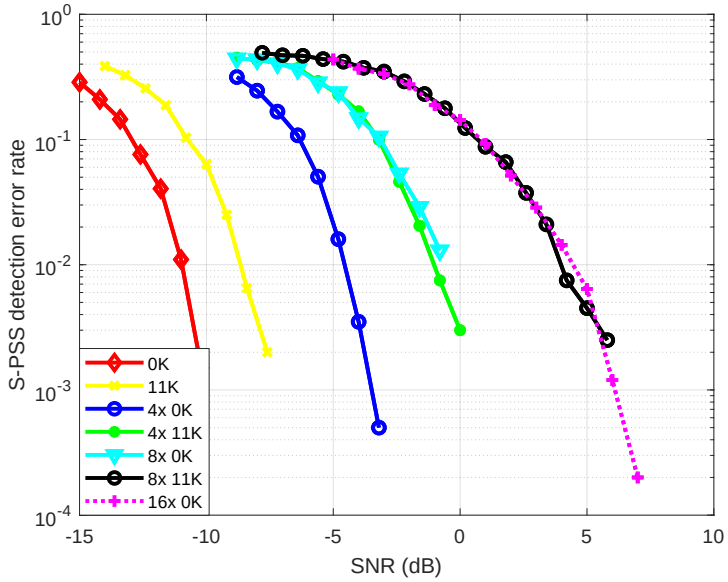

Figure 17. Detection performance of S-PSS.

 doi:10.20944/preprints202602.1239.v1

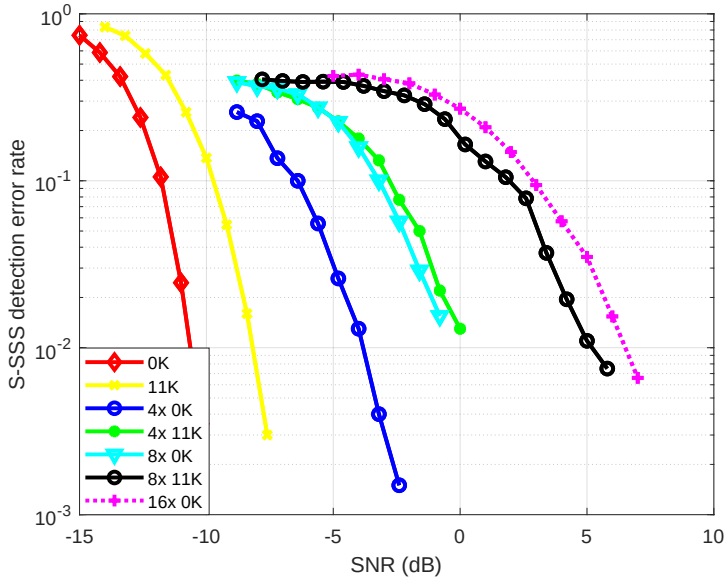

Figure 18. Detection performance of S-SSS.

Frequency offsets also exert an impact on detection performance: in the case where no downsampling is applied, the degree of performance degradation caused by an 11 KHz frequency offset is lower than that caused by application of 4× downsampling. When the downsampling factor is less than 4×, reduction in sampling quantity is the main cause of performance loss; when the downsampling factor reaches 4× or higher (e.g., 4× downsampling), the performance degradation caused by additional application of an 11 KHz frequency offset is equivalent to that caused by an additional 2× downsampling (i.e., the total downsampling factor reaches 8×). Thus, after 4× downsampling, the impact on performance from an 11 KHz frequency offset is identical to that from 2× downsampling.

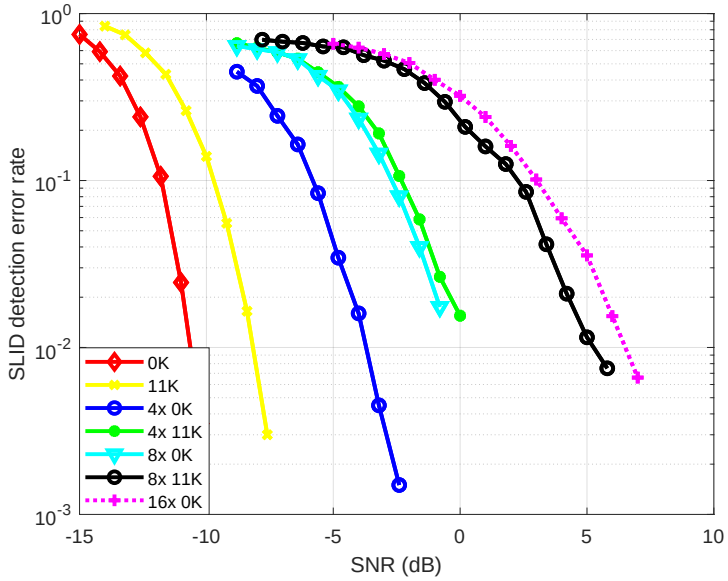

Figure 19. Detection performance of SLID.

The demodulation performance of the payload is presented in Figure 20. For payload demodulation, 4× downsampling during the S-PSS detection phase does not cause significant performance degradation, which is because the original synchronization detection performance is far higher than the performance level required for payload demodulation. However, synchronization performance after 4× downsampling is severely weakened by frequency offsets, thereby reducing the payload

 doi:10.20944/preprints202602.1239.v1

demodulation quality. In payload detection, it is also confirmed that an 11 KHz frequency offset and an additional 2× downsampling have an equivalent impact.

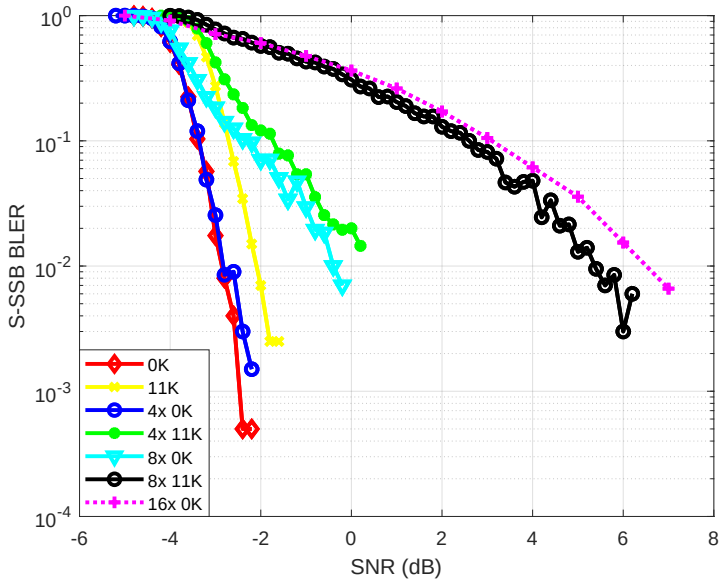

Figure 20. Demodulation performance of S-SSB.

5. Conclusions

In this paper, for the uplink synchronization between the ground base station and the relay node, the problem that the current 5G preamble design cannot meet the ultra-long-distance synchronization requirement is addressed. Based on the 5G preamble structure, a modified preamble structure and an improved two-step detection framework are introduced. Through the transmission strategy of sending preambles with two different root sequences, RTD estimation and preamble detection are achieved under the condition that the transmission delay is much longer than the length of traditional 5G preambles. This breakthrough overcomes the limitation of the preamble structure on communication distance in long-distance access. Meanwhile, it is compatible with the existing 5G preamble sequences to realize a smooth transition, providing a reliable technical guarantee for communication coverage enhancement.

Regarding the uplink synchronization problem between the relay node and slave nodes, this paper focuses on the two core contradictions of efficiency and interference in high-dynamic scenarios, and constructs a two-step random access scheme based on A-NOMA. On one hand, the existing 5G preamble sequences are utilized to construct a paired-index preamble design, through which the Doppler frequency offset and time offset caused by high-speed movement are estimated, facilitating the subsequent demodulation of the PUSCH. On the other hand, for the demodulation of asynchronous NOMA, a demodulation algorithm based on phase and frequency offset compensation is proposed, which effectively suppresses the interference of asynchrony and frequency offset on demodulation. Without occupying additional resources, this design improves the access efficiency under the conditions of frequency offset and asynchrony.

In terms of downlink synchronization between the relay node and slave nodes, the practical constraint of limited on-board energy of UAVs is taken into account. This paper addresses the issue from two aspects: reducing power consumption and adapting to scenarios. A downlink synchronization detection scheme based on downsampling is proposed, which reduces the energy consumption of downlink synchronization while ensuring synchronization accuracy. In addition, the resource allocation of the S-SSB in sidelink communication is redesigned, and a complete link-level algorithm is constructed. This enables the system to be better adapted to the high-dynamic and wide-coverage UAV communication scenarios.

 doi:10.20944/preprints202602.1239.v1

References

1. Salvador, L. R.; Rajnai, Z.; 5G Standardization Process: An Overview. In Proceedings of 2023 IEEE 21st Jubilee International Symposium on Intelligent Systems and Informatics (SISY), Pula, Croatia, 26–28 Oct 2023.
2. Zhang, P.; Yang, X.; Chen, J.; Huang, Y.; A survey of testing for 5G: Solutions, opportunities, and challenges. *China Communications* **2019**, *16*, 69-85.
3. Hassan, M. S.; Saha, C.; Ji, L.; Alvarino, A.R.; Ma, J.; Liu, L.; Wu, Q.; NTN: from 5G NR to 6G. In Proceedings of 2023 IEEE International Conference on Wireless for Space and Extreme Environments (WiSEE), Aveiro, Portugal, 6-8 Sept 2023.
4. Wang, C.; You, X.; Gao, X.; Zhu, X.; Li, Z.; Zhang, C.; Wang, H.; Huang, Y.; Chen, Y.; Haas, H.; Thompson, J.S.; Larsson, E.G.; Renzo, M.D.; Wen, T.; Zhu, P.; Shen, X.; Poor, H.V.; Hanzo, L.; On the Road to 6G: Visions, Requirements, Key Technologies, and Testbeds. *IEEE Communications Surveys & Tutorials* **2023**, *25*, 905-974.
5. Danuti, F.; Otesteanu, M.; 6G: An Overview of Key Technologies and Challenges. In Proceedings of 2024 International Symposium on Electronics and Telecommunications (ISETC), Timisoara, Romania, 7-8 Nov 2024.
6. Shahid, H.; Amatetti, C.; Campana, R.; Tong, S.; Panaitopok, D.; Vanelli-Coralli, A.; Mohamed, A.; Zhang, C.; Khalifa, E.; Medeiros, E.; Recayte, E.; Ghasemifard, F.; Ji, L.; Bucheli, J.; Caus, M.; Gurelli, M.; Vazquez, M.A.; Shaat, M.; Borios, N.; Eriksson, P.E.; Euler, S.; Li, Z.; Fu, X.; Emerging Advancements in 6G NTN Radio Access Technologies: An Overview. In Proceedings of 2024 Joint European Conference on Networks and Communications & 6G Summit (EuCNC/6G Summit), Antwerp, Belgium, 3-6 June 2024.
7. Medina-Acosta, G.A.; Mungara, R.K.; Eriksson, S.G.; Khan, T.; 3GPP Release-18 Physical Layer Enhancements for IoT-NTN. *IEEE Communications Standards Magazine* **2024**, *8*, 18-24.
8. Mitra, R.N.; Rong, B.; 5G Non-Terrestrial Networks: Technologies, Standards, and System Design. *IEEE Wireless Communications* **2024**, *31*, 14-14.
9. Giordani, M.; Polese, M.; Mezzavilla, M.; Rangan, S.; Zorzi, M.; Toward 6G Networks: Use Cases and Technologies. *IEEE Communications Magazine* **2020**, *58*, 55-61.
10. Parzysz, F.; Guidotti, A.; Vanelli-Coralli, A.; Measuring Service Continuity in Integrated TN/NTN for 5G-Advanced and 6G. In Proceedings of 2022 13th International Conference on Information and Communication Technology Convergence (ICTC), Jeju Island, Korea, 3-6 June 2024.
11. Zhang, Z.; Guo, H.; Xie, W.; Research of NTN Technical Scheme Based on 5G Network. In Proceedings of 2023 IEEE International Symposium on Broadband Multimedia Systems and Broadcasting (BMSB), Beijing, China, 14-16 June 2023.
12. Cao, L.; Wang, H.; Research on UAV Network Communication Application Based on 5G Technology. In Proceedings of 2022 3rd International Conference on Electronic Communication and Artificial Intelligence (IWECAI), Zhuhai, China, 14-16 Jan 2022.
13. Azari, M.M.; Solanki, S.; Chatzinotas, S.; Kodheli, O.; Sallouha, H.; Colpaert, A.; Montoya, J.F.M.; Pollin, S.; Haqiqatnejad, A.; Mostaani, A.; Lagunas, E.; Ottersten, B.; Evolution of Non-Terrestrial Networks From 5G to 6G: A Survey. *IEEE Communications Surveys & Tutorials* **2022**, *24*, 2633-2672.
14. Yamamoto, S.; Nakazato, J.; Tran, G.K.; Study on the Coverage Extension of Millimeter Wave UAV BS Networks by Using IRS. In Proceedings of 2024 IEEE 21st Consumer Communications & Networking Conference (CCNC), Las Vegas, NV, USA, 6-9 Jan 2024.
15. Hosseinian, M.; Choi, J.P.; Chang, S-H.; Lee, J.; Review of 5G NTN Standards Development and Technical Challenges for Satellite Integration With the 5G Network. *IEEE Aerospace and Electronic Systems Magazine* **2021**, *36*, 22-31.
16. Keefe, A.; Iyer, S.; Demonstration of Advanced Regenerative 5G NTN NR Satellite Base Station Prototype. In Proceedings of MILCOM 2024 - 2024 IEEE Military Communications Conference (MILCOM), Washington, DC, USA, 28 Oct – 1 Nov 2024.
17. S. Krishna M, P. K. N.; Balasubramanya, N. M.; Performance Analysis of a UAV-based Non-Terrestrial Network (NTN) using NB-IoT. In Proceedings of 2023 IEEE Wireless Communications and Networking Conference (WCNC), Glasgow, United Kingdom, 26-29 March 2023.
18. Lin, X.; Rommer, S.; Euler, S.; Yavuz , E.A.; Karlsson , R.S.; 5G from Space: An Overview of 3GPP Non-Terrestrial Networks. *IEEE Communications Standards Magazine* **2021**, *5*, 147-153.
19. Kim, J.; Kim, C.; A Study on Hybrid Content Delivery using NTN and MBS in 5G Network. In Proceedings of 2024 Joint European Conference on Networks and Communications & 6G Summit (EuCNC/6G Summit), Antwerp, Belgium, 19-21 Oct 2022.

 doi:10.20944/preprints202602.1239.v1

20. Cao, L.; Wang, H.; Research on UAV Network Communication Application Based on 5G Technology. In Proceedings of 2022 3rd International Conference on Electronic Communication and Artificial Intelligence (IWECAI), Zhuhai, China, 14-16 Jan 2022.
21. Min, Y.; Jiaji, Z.; Key technologies of physical layer of radio and television wireless network based on 5g wireless communication network. In Proceedings of 2022 World Automation Congress (WAC), San Antonio, TX, USA, 11-15 Oct 2022.
22. Xiao, Z.; Zhu, L.; Xia, X.G.; UAV communications with millimeter-wave beamforming: Potentials, scenarios, and challenges. *China Communications* **2020**, *17*, 147-166.
23. Nguyen, T.H.; Park, L.; Multi-agent DRL-based Task Offloading in Hierarchical HAP-LAP Networks. In Proceedings of 2022 13th International Conference on Information and Communication Technology Convergence (ICTC), Jeju Island, Korea, 19-21 Oct 2022.
24. Zhang, L.; Zhao, H.; Hou, S.; Zhao, Z.; Xu, H.; Wu, X.; Wu, Q.; Zhang, R.; A Survey on 5G Millimeter Wave Communications for UAV-Assisted Wireless Networks. *IEEE Access* **2019**, *7*, 117460-117504.
25. Benouadah, S.; Mishra, L.; Kaabouch, N.; Zhang, R.; Doppler Shift Effect on Bandwidth Availability for UAV Communications. *IEEE Access* **2019**, *7*, 117460-117504.
26. Qi, W.; Wang, H.; Xia, X.; Survey on Security Analysis in RIS-Assisted the Space-Air-Ground Integrated Network. In Proceedings of 2023 International Conference on Information Processing and Network Provisioning (ICIPNP), Beijing, China, 26-27 Oct 2023.
27. Kim, Y.J.; Choi, S.; Cho, Y.S.; New Random Access Preamble Design Technique for Non-Terrestrial Networks With High Doppler Shift. *IEEE Transactions on Vehicular Technology* **2025**, *74*, 11579-11584.
28. Wang, Y.; Jiang, Y.; Zhao, L.; Preamble Design for LEO Satellite Communication System. In Proceedings of 2023 28th Asia Pacific Conference on Communications (APCC), Sydney, Australia, 19-22 Nov 2023.
29. Jiao, X.; Tang, X.; Hao, L.; Preamble Sequence Design in Frequency offset Channel for mMTC Scenarios. In Proceedings of 2023 6th International Conference on Electronics Technology (ICET), Chengdu, China, 12-15 May 2023.
30. Wang, L.; Wang, M.M.; Zhang, J.; Preamble Detection Performance of LoRa Under Low-Complexity Receiver. *IEEE Wireless Communications Letters* **2024**, *13*, 2357-2361.
31. Chen, H.; Wang, P.; Li, S.; Lin, S.; Wang, Z.; Fang, C.; A Novel Preamble Design for 5G Enabled LEO Non-Terrestrial Networks. In Proceedings of GLOBECOM 2022 - 2022 IEEE Global Communications Conference, Rio de Janeiro, Brazil, 4-8 Dec 2022.
32. Zhen, L.; Sun, T.; Liu, G.; Yu, K.; Ding, R.; Preamble Design and Detection for 5G Enabled Satellite Random Access. *IEEE Access* **2020**, *8*, 49873-49884.
33. He, W.; Jiang, Y.; Zhao, L.; Random Access Preamble Design and Detection for Mobile Satellite Communication Systems. In Proceedings of 2024 IEEE/CIC International Conference on Communications in China (ICCC), Hangzhou, China, 7-9 Aug 2024.
34. Zhang, C.; Cao, W.; Zhang, N.; Tian, K.; Li, R.; Root Pair Selection for Two-root Random Access Preamble. In Proceedings of 2021 IEEE 93rd Vehicular Technology Conference (VTC2021-Spring), Helsinki, Finland, 25-28 Apr 2021.
35. Condoluci, M.; Dohler, M.; Araniti, G.; Molinaro, A.; Sachs, J.; Enhanced Radio Access and Data Transmission Procedures Facilitating Industry-Compliant Machine-Type Communications over LTE-Based 5G Networks. *IEEE Wireless Communications* **2016**, *23*, 56-63.
36. Kim, T.; Chae, S.H.; Bang, I.; Performance Evaluation of Two-Step Random Access for Low-Latency Communications in 6G. In Proceedings of 2024 Fifteenth International Conference on Ubiquitous and Future Networks (ICUFN), Budapest, Hungary, 2-5 July 2024.
37. Nie, D.; Yu, W.; Foh, C.; Ni, Q.; A NOMA-Enhanced Two-Step RACH Procedure for Low-Latency Access in 5G Networks. *IEEE Internet of Things Journal* **2025**, *12*, 11568-11580.
38. Song, S.; Seo, J.B.; Jin, H.; Online Control of Two-Step Random Access: A Step Towards uMTC. In Proceedings of 2023 IEEE Wireless Communications and Networking Conference (WCNC), Glasgow, United Kingdom, 26-29 March 2023.
39. Yang, J.; Yang, X.; Wang, H.; Two-Step Random Access Using Spatial Grouping and User Paring in Satellite Communication Systems. In Proceedings of 2022 IEEE 8th International Conference on Computer and Communications (ICCC), Chengdu, China, 9-12 Dec 2022.
40. You, Y.; Lee, S.; Lee, K.; Effective Time, Frequency, and Sidelink Synchronization for Cellular Device-to-Device Communications. *IEEE Systems Journal* **2021**, *15*, 2938-2947.

 doi:10.20944/preprints202602.1239.v1

41. Jang, D.; Jo, S.; Kim, G.; Bea, J.; Choi, T.; Kim, T.; Link-Level Performance Evaluation of Sidelink Synchronization Signal Block for 5G V2X. In Proceedings of 2023 Fourteenth International Conference on Ubiquitous and Future Networks (ICUFN), Paris, France, 4-7 July 2023.
42. Uemori, S.; Okura, R.; Koda, Y.; Harada, H.; Highly-Efficient Sidelink SSB Format and Synchronization Algorithm for Common-Mode Signaling in 5G NR Sidelink-Based mmWave WPAN Systems. In Proceedings of 2025 IEEE Wireless Communications and Networking Conference (WCNC), Milan, Italy, 24-27 March 2025.
43. Zhang, H.; Chen, H.-M.; Fang, C.; Wang, S.-F.; Wei, Q.-J.; Sun, Y.-H. Design of Asynchronous NOMA-Driven Two-Step Random Access for Subspace UAVs. In Proceedings of the 11th International Conference on Computer and Communications (ICCC) (Unpublished), Chengdu, China, 12-15 December 2025; *presented*.